

Article

Catalytic Effect of NaCl on the Improvement of the Physicochemical Structure of Coal-Based Activated Carbons for SO₂ Adsorption

Dongdong Liu ¹ , Rui Su ¹, Zhengkai Hao ¹, Xiaoman Zhao ¹, Boyin Jia ^{2,*} and Liangjie Dong ¹

¹ College of Engineering and Technology, Jilin Agricultural University, Changchun 130118, China; liudongdong@jlau.edu.cn (D.L.); gaojihui0809@163.com (R.S.); hzk980924@163.com (Z.H.); zhaoxiaoman0930@163.com (X.Z.); jiaboyinjby@163.com (L.D.)

² College of Animal Science and Technology, Jilin Agricultural University, Changchun 130118, China

* Correspondence: jiaboyin@jlau.edu.cn

Received: 25 April 2019; Accepted: 28 May 2019; Published: 5 June 2019



Abstract: The utilization of coal-based activated carbons focuses on improving the physicochemical structure for achieving high-capacity. Herein, the catalytic effect of NaCl (1 and 3 wt%) in the presence of oxygen functional groups on the improvement of the physicochemical structure of coal-based activated carbons is studied in this work. A large quantity of Na can be retained in 1NaJXO and 3NaJXO with the presence of oxygen functional groups to promote further its catalytic characteristics during pyrolysis, resulting in the disordered transformation of the carbon structure. In addition, the development of micropores is mainly affected by the distribution and movement of Na catalyst, whereas the growth of mesopores is mainly influenced by the evolution of oxygen functional groups. Then, the active sites of 3NaJXO-800 can no longer be consumed preferentially in the presence of Na catalyst during subsequent CO₂ activation to facilitate the sustained disordered conversion of the microstructure and the rapid development of the micropores, resulting in the obvious high S_{BET} value as activation proceeds. And the high S_{BET}/burn-off ratio value (41.48 m²·g⁻¹/%) of 3NaJXO-800 with a high value of S_{BET} (1995.35 m²·g⁻¹) at a low burn-off value (48.1%) can be obtained, presenting the high efficiency of pore formation. Finally, the SO₂ adsorption efficiency of 3NaJXO-800-48.1 maintains at 100% within 90 min. After 180 min, 3NaJXO-800-48.1 still presents a high adsorptive capacity (140.2 mg/g). It is observed that a large micropore volume in the case of hierarchical pore structure necessarily assures optimal adsorption of SO₂.

Keywords: activated carbons; catalytic activation; physicochemical structure; SO₂ adsorption

1. Introduction

Recently, gas sorption, storage and separation in porous nanocarbons and metal–organic frameworks have received increasing attention. In particular, the tunable porosity, surface area and functionality of the lightweight and stable graphene-based materials open up great scope for those applications [1]. Activated carbons (ACs) as an adsorbent material is a promising choice to achieve the gas pollutants (such as SO₂, NO_x) adsorption [2]. In the case of ACs, the gas pollutants are adsorbed and catalyzed in abundant active sites within micropores, then can be further migrated and stored in developed mesopores [3], so the effective removal of gas pollutants is closely related to the physicochemical structure of ACs, including more amounts of active sites, a hierarchical distribution of pores and a high specific surface area (S_{BET}). Among some synthesis methods (such as physical or chemical activation [4], soft/hard template [5,6], hydrothermal carbonization and self-assembly [7,8]) and sources of raw materials (such as coal, biomass, wastes, MOF and ordered mesoporous carbons),

the traditional physical activation using H₂O, CO₂, flue gas, or their mixtures as activation agents can partially etch the carbon-based framework to obtain desirable porosity and more active sites over other methods, in addition, the coal as the most suitable raw materials instead of other materials can satisfy the industrial application of ACs [9]. Therefore, coal-based ACs produced by physical activation process meets the requirements of economic and environmental friendliness.

In order to improve the physicochemical structure of coal-based ACs, some researchers concentrate mainly on various activation modes (such as the single activation and mixing activation) [10,11]. However, the obtained products present the low S_{BET} values between 600 and 1000 m²/g at the high burn-off value of approximately around 60–85% and the rapid consumption of active sites during activation, finally resulting in a higher cost [12–16]. Thus, it is difficult to obtain the ideal AC only by adjusting the activation conditions during activation. Our previous research found that the number of initial pores and active sites of chars produced by pyrolysis and the disordered conversion of carbon structure of chars during activation have important effects on the ideal AC production [17]. Furthermore, more initial pores can promote rapidly the diffusion of the activated gas into the particles' interior to avoid external loss of quality effectively, resulting in the high efficiency of pore formation. In addition, a lot of active sites and the disordered conversion of carbon structure at high activation temperatures can further promote etching of carbon-based framework to obtain desirable porosity and more new active sites.

Alkali metals (such as Na and K) in raw coal play an efficient catalytic role in gasification which is similar to physical activation reaction, and the corresponding catalytic mechanism has been investigated by some researchers [18–22]. Alkali metal not only can fundamentally change the reaction path between activated gas and active sites, but also can accelerate the reaction between the active gas and coal matrix by providing catalytic active sites, finally, the increase of new active sites and the disordered conversion of carbon structure during gasification. Importantly, most of the works in the literature reported that large amounts of alkali metals have been released into the gas phase during the temperature range of 300–900 °C, resulting in the absence of a large number of catalyst in the subsequent activation stage [23–27]. However, some studies also reported that the introduction of oxygen functional groups play an important role in the movement and catalytic effect of alkali metals [28–30]. Alkali metals (M) can be fixed inside char during pyrolysis as intermediates (such as C-O-M and -COOM) form which act as catalytic active sites to react with activated gas at the activation stage. In addition, in our previous study [31] and Francisco et al. [32] found that more active sites in chars can be produced by the introduction of oxygen functional groups during pyrolysis.

In this work, we systematically investigated the catalytic effect of alkali metal under the introduction of oxygen functional groups regarding the improve of the physicochemical structure of Jixi bituminous coal-based activated carbons. A series of samples were prepared by loading various amounts of the NaCl (1 wt% and 3 wt%) and/or the subsequent pre-oxidation in the air at 200 °C for 48 h. To verify the application potentials of the ideal activated carbons with developed pore structure, SO₂ removal tests also were conducted by portable FTIR. The characteristic parameters of all samples were determined by scanning electron microscopy (SEM), nitrogen adsorption, X-ray diffraction (XRD) and Raman spectroscopy.

2. Materials and Methods

2.1. Materials

Jixi bituminous coal was collected from the southeast of Heilongjiang province in China, and acted as the source material for the preparation of ACs. Different particle sizes of 250–380 μm from the Jixi bituminous coal were obtained through crushing and sieving. Importantly, the raw materials were demineralized sequentially using 6 mol·L⁻¹ HCl and 40 wt% HF [33]. Afterwards, the sample was treated with deionized water and dried in an oven at 80 °C overnight. After that, the proximate and ultimate analysis of a demineralized sample (denoted as JX) were shown in Table 1.

Table 1. Proximate and ultimate analyses of JX (wt%).

V _{ad}	FC _{ad}	A _{ad}	M _{ad}	C _{daf}	H _{daf}	O _{daf} *	N _{daf}	S _{daf}
39.66	56.60	0.12	3.62	74.81	19.49	4.01	1.31	0.38

* By difference; ad (air-dried basis): The coal in dry air was used as a benchmark; daf (dry ash free basis): The remaining component after the removal of water and ash in coal was used as a benchmark.

Na-loaded samples were prepared by liquid impregnation. A known amount of NaCl powder was first added into a beaker and dissolved by deionized water under magnetic stirring. NaCl powder was obtained from Kemiou, Tianjin, China. A pre-weighed amount of JX was then added into the beaker to make a coal-water slurry. The coal-water slurry was dried at 80 °C with magnetic stirring of 300 r/min, until the water was completely evaporated. The mass content of Na in the mineral-loaded coal samples is controlled at 1 wt% and 3 wt%. The Na-loaded samples were denoted as 1NaJX and 3NaJX. In addition, JX was oxidized in air at 200 °C for 48 h, the oxidized sample was marked as JXO. Then, a predetermined amount of NaCl powder (0.03 g and 0.09 g) and 3 g of JXO were mixed using above liquid impregnation to prepare the Na-loaded oxidized samples and they were marked as 1NaJXO and 3NaJXO.

2.2. Experimental Process

The 3 g of samples were heated at a constant rate of 10 °C/min in nitrogen (99.999%) flow of 300 mL/min by the three-stage fixed-bed reactor. Thermal upgrading stopped when the final temperature reached 300, 400, 500, 600, 700, 800, 900 and 1000 °C then maintained for 10 min, and after that, the samples were quickly cooled in a nitrogen atmosphere and was marked as JX, JXO, 1NaJX, 3NaJX, 1NaJXO and 3NaJXO- pyrolysis temperature. After that, the atmosphere was switched to CO₂ (99.999%) at the same flow rate for a certain time to produce ACs with different porous structures, which were marked as the samples-pyrolysis time—burn-off value. In order to eliminate the interference of Na-based compounds in chars for the results of XRD and Raman. The 10 g of testing samples, including Na-based compounds were washed with 300 mL of 0.2 mol L⁻¹ HCl at 60 °C for 24 h using magnetic stirring, then the residual acid-soluble inorganic salts on the surface of coal particles were removed by filtering and washing with 300 mL deionized water twice, respectively. In addition, the dissolved Na element in the residual liquid was quantified by an ICP-AES. This testing process was repeated three times, and the test results were averaged.

2.3. Measurement Analysis

The visualized results of surface topography of samples were obtained by SEM (Quanta 200, FEI, Hillsboro, OR, USA) at 200 kV. The crystal parameters of the samples were obtained by a D/max- rb X-ray diffractometer (XRD, D8 ADVANCE, Brooke, Karlsruhe, Germany) in the 2 θ range from 10° to 80°, and the scanning rate of XRD was set at a stable value of 3°/min. The different hybrid carbon structures of the samples were obtained by Raman spectroscopy via a 532 nm wavelength laser, and the scanning scope was determined from 1000–1800 cm⁻¹. The information of pore structure was obtained by a micromeritics adsorption apparatus (ASAP2020, Micromeritics, Norcross, GA, USA) in a relative pressure (P/P_0) range from 10⁻⁷ to 1, and the analysis temperature was set at 77 K [34]. The vacuum degassing process for samples was performed before the test and analysis experiment, and the temperature and time were set to 473 K and 12 h. Furthermore, the specific parameters of pore structure, such as the specific surface area (S_{BET}), the micropore area (S_{mic}), and the micropore volume (V_{mic}), were calculated using the following formulas: Brunauer–Emmett–Teller (BET) equation, the t-plot method, Horvath–Kawazoe (HK) method, and nonlocal density functional theory (NLDFT), respectively [35]. In addition, the parameter of the total pore volume (V_t) was obtained at 0.98 relative pressure. Elemental analysis (EA) was performed using an analyzer (Vario MACRO cube, Elementar, Langenselbold, Germany) for determination of the total carbon and oxygen content of the bulk samples.

The quantification of sodium was obtained by an ICP-AES (Optima 5300 DV, PerkinElmer, Boston, MA, USA).

2.4. The SO₂ Adsorption Test

The SO₂ adsorption experiments were carried out in a fixed bed reactor using an on-line Fourier transform infrared gas analyzer (Dx4000, Gasmeter, Vantaa, Finland) to continuously monitor the SO₂ concentrations. The experimental system consists of a tubular reactor (20 mm diameter), placed in a vertical furnace, with a system of valves and mass flow controllers in order to select the flow and the composition of the inlet gas, as shown in Figure S1. In each typical running, 2.5 g of the sample was put into the tubular reactor at 80 °C within 120 min. The gas volumetric composition used in experiments was: SO₂, 1500 ppm; O₂, 5%; water vapor, 10%; N₂, balance, total flow rate 200 mL·min⁻¹. SO₂ removal efficiency and rate versus time were evaluated by detected concentrations of SO₂ at the inlet and outlet in real time through the gas analyzer. The SO₂ removal capacity of coal-based activated carbons was calculated by the integrating area above the removal curves and reaction time [36].

3. Results and Discussion

3.1. Sodium Release of NaCl Loaded Chars at Pyrolysis

Figure 1 shows the retention of Na (%) in different chars during pyrolysis. With the increase of pyrolysis temperature, the retention of Na in the char all decreases.

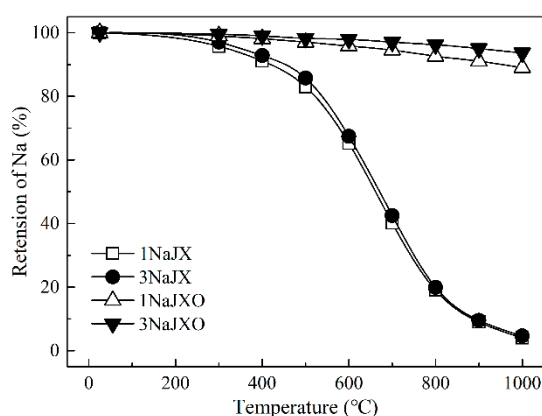


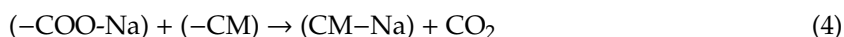
Figure 1. The retention of Na (%) in different chars at pyrolysis.

The trends of the retention of Na in 1NaJX and 3NaJX are similar, especially when the pyrolysis temperature is higher than 500 °C, the retention of Na rapidly decrease from 85 to 5%, indicating the release of Na from chars cannot be changed only by adding the amount of catalyst. Li et al. 26 found that the repeated fracture and recombination processes are presented between alkali metal and coal/coke system (CM), resulting in the production of more stable chemical bonds as the increase of pyrolysis temperature, the entire reaction process can be expressed as follows:



In addition, it is noteworthy that large quantities of Na are retained in 1NaJXO and 3NaJXO during pyrolysis. Some intermediates (such as -O-Na and -COONa) are formed to fix Na within chars in the temperature range from 300 °C to 600 °C, resulting in the release of a small amount of sodium. Then these intermediates with low thermal stability (such as -COONa) may further be dissociated

into the volatile matter to produce more active sites, promoting the re-bonding process between Na and carbon matrix (CM), the reaction process can be expressed as follows [37]:



However, other intermediates with high thermal stability ($-\text{O}-\text{Na}$) can continue to stabilize alkali metal Na within chars even at a higher temperature.

3.2. Carbon Structure Analysis of Chars at Pyrolysis

The Raman spectra of the different chars are shown in Figure S2. To obtain more information about the hybrid carbon structure of chars, each Raman spectrum was treated further into five band areas by the fitting method [38]. Importantly, the ratios of the different band areas, such as A_{D1}/A_G , A_{D3}/A_G , A_{D4}/A_G , and A_{D1}/A_{D3} , represent the different types of hybrid carbon as follow in turn: The defect degree of the microcrystalline structure; the amorphous carbon; the relative quantity of cross-linking bonds; the ratio between big rings relative to small fused rings in chars [39,40]. The parameters of the carbon structure of carbonized chars are given in Figure 2.

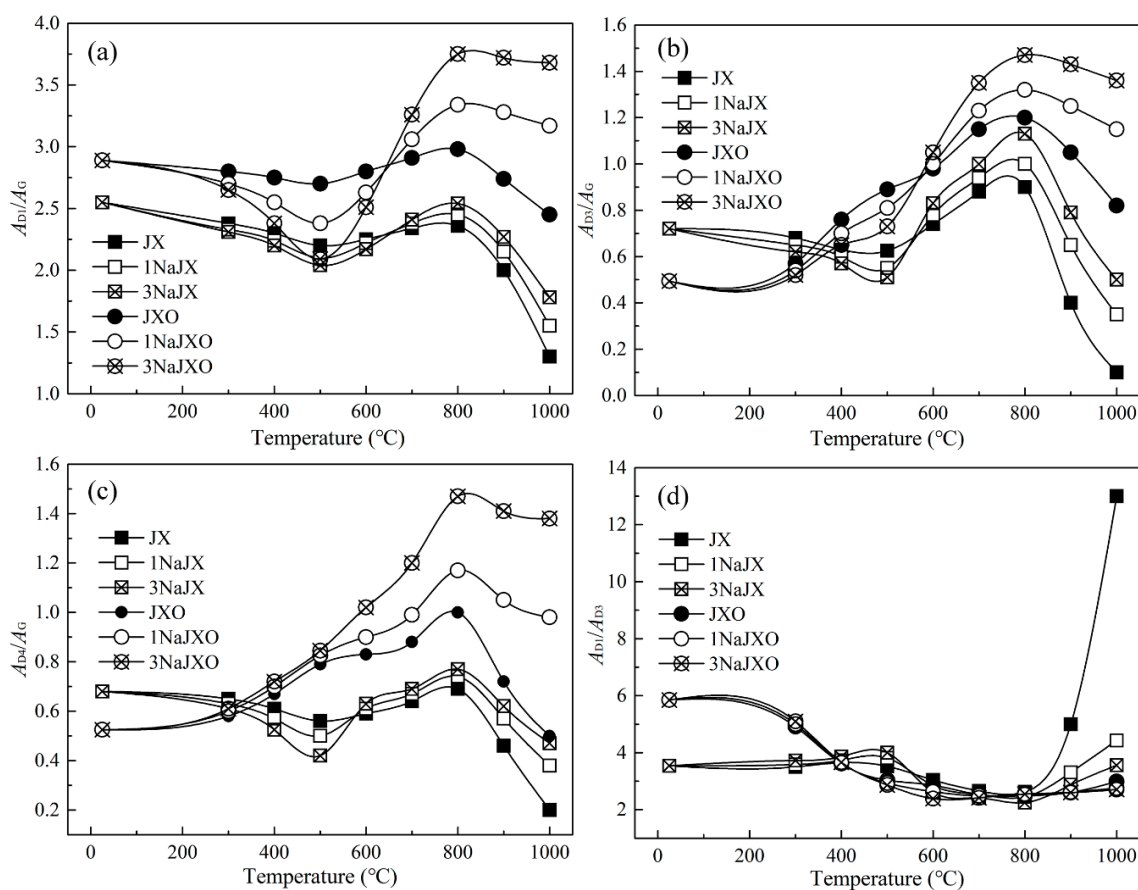


Figure 2. Raman data from chars at pyrolysis (a) A_{D1}/A_G ; (b) A_{D3}/A_G ; (c) A_{D4}/A_G ; (d) A_{D1}/A_{D3} .

First of all, the values of A_{D1}/A_G , A_{D3}/A_G and A_{D4}/A_G of JX, 1NaJX and 3NaJX decrease obviously with the increase of Na loading during temperature rising from 25 to 500 °C, whereas the A_{D1}/A_{D3} value increases gradually. These results indicate that the splitting of big aromatic rings (A_{D1}/A_G) and the remove of a large number of amorphous sp^2 bonding carbon atoms (A_{D3}/A_G) as volatile matter at the beginning of pyrolysis result in the increase in the A_{D1}/A_{D3} value. Moreover, these reactions can be further strengthened under the presence of Na. The value of A_{D3}/A_G of 1NaJX and 3NaJX continues to decrease in this stage, due to the release of more organic components caused by the catalytic

decomposition of Na. Alternatively, the value of A_{D1}/A_G decreases slightly and A_{D1}/A_{D3} decrease quickly, whereas the values of A_{D3}/A_G and A_{D4}/A_G of JXO increase obviously. The cross-linking reaction of oxygen-containing functional groups not only promotes the formation of cross-linking bonds (such as -COO- and -O-) and more small aromatic rings (such as some oxygen-containing heterocycles), but hinders the intense decomposition of aromatic structure. However, the values of A_{D1}/A_G and A_{D1}/A_{D3} decrease obviously and the A_{D3}/A_G and A_{D4}/A_G of 1NaJXO and 3NaJXO increase slightly as compared with that of JXO. The formation of some intermediates can fix Na within chars to promote further its catalytic decomposition and reduce the number of cross-linking bonds.

Then, the values of A_{D1}/A_G , A_{D3}/A_G and A_{D4}/A_G of JX, 1NaJX and 3NaJX increase obviously with the increase of Na loading during temperature rising from 500 to 800 °C, whereas the A_{D1}/A_{D3} value decreases gradually. The increase of some aromatic rings originates from the formation of more new cross-linking bonds at this stage. Especially, there is no significant change in all parameters for JX from 700 to 800 °C, where the process of cross-linking reaction can be shortened to hinder the production of sp^2 - sp^3 bonding carbon atoms; the amorphous sp^2 bonding carbon atoms and transformation of small aromatic rings to form big aromatic rings, these results indicate the—graphitization conversion of microcrystalline. In addition, a large amount of Na is released as volatile, the remaining Na is bonded to carbon matrix (CM) to form the stable chemical bonds (CM-Na) at high temperature during which more free radical fragments have been produced. Thus, the cross-linking reaction can be strengthened continuously accompanied by the combination of free radical fragments, resulting in an obvious increase in all parameters of 1NaJX and 3NaJX. The values of A_{D1}/A_{D3} , A_{D1}/A_G , A_{D3}/A_G and A_{D4}/A_G of JXO increase at this stage. The break of oxygen-containing structures with low thermal stability not only helps the production of new cross-linking bonds with high thermal stability to form furthermore small aromatic rings, but also promotes the transformation of small aromatic rings to big aromatic rings. However, the value of A_{D1}/A_{D3} of 1NaJXO and 3NaJXO decreases, and the values of A_{D1}/A_G , A_{D3}/A_G and A_{D4}/A_G continue to increase than that of JXO. The retention of more Na caused by the existence of oxygen-containing structures enhances further the catalytic and cross-linking reaction, resulting in the higher activity of coal chars.

Finally, the values of A_{D1}/A_G , A_{D3}/A_G and A_{D4}/A_G of JX decrease obviously, whereas the A_{D1}/A_{D3} value increases from 800 to 1000 °C, and the change range of the corresponding parameters of 1NaJX, 3NaJX, JXO, 1NaJXO and 3NaJXO reduces gradually. These results indicate the relevant reactions (including the break of cross-linking bonds; the transformation of the isolated sp^2 structure and the amorphous sp^2 bonding carbon atoms into the crystalline sp^2 structure) all are promoted at higher pyrolysis temperature, presenting the more ordered conversion of carbon structure with lower reactivity. In addition, the change of A_{D1}/A_{D3} value indicates that the amorphous sp^2 bonding carbon atoms are more easily transformed into the crystalline sp^2 structure (G peak). In particular, Na can promote further the stability of some oxygen-containing structures to hinder the graphitization conversion of the carbon structure.

3.3. Crystal Structure Analysis of Coal Chars at Pyrolysis

The XRD profiles of the different chars are shown in Figure S3. Some important structure feature information of aromatic layers (such as layer distance (d_{002}), stacking height (L_c) and width (L_a)) can be obtained through the fitting treatment of two obvious broad diffraction peaks at $2\theta = 24^\circ$ – 27° and 41° – 44° in all samples [41]. The results of themicrocrystalline structure are shown in Figure 3.

First of all, the L_a value of JX, 1NaJX and 3NaJX decreases and the L_c value first decreases and then increases, and the d_{002} first increases and then decreases from 25 to 500 °C. These changes may be related to the break of chemical bonds and the release of organic fragments (such as $\bullet C_n H_{2n+1}$, $\bullet OC_n H_{2n+1}$, and substituted benzene) [41]. The break of chemical bonds and the slow release of organic fragments facilitate the production of the metaplast material, resulting in the movement, the orientation adjustment and the stacking of aromatic layers (namely the presence of a plastic behavior) for JX. However, the addition of NaCl accelerates the depolymerization of aromatic structure unit to produce

more volatile matters and the smaller the aromatic structure, which weakens the production of the metaplast material, the movement and the stacking of aromatic layers [42]. Alternatively, the values of L_a , L_c and d_{002} of JXO, 1NaJXO and 3NaJXO increase. The growth and stacking of aromatic layers are promoted by cross-linking reaction of oxygen-containing functional groups, and the significant reductions of organic fragments during the pre-oxidation stage is beneficial to the increase of the layer distance, whereas the formation of some intermediates can reduce the number of cross-linking bonds.

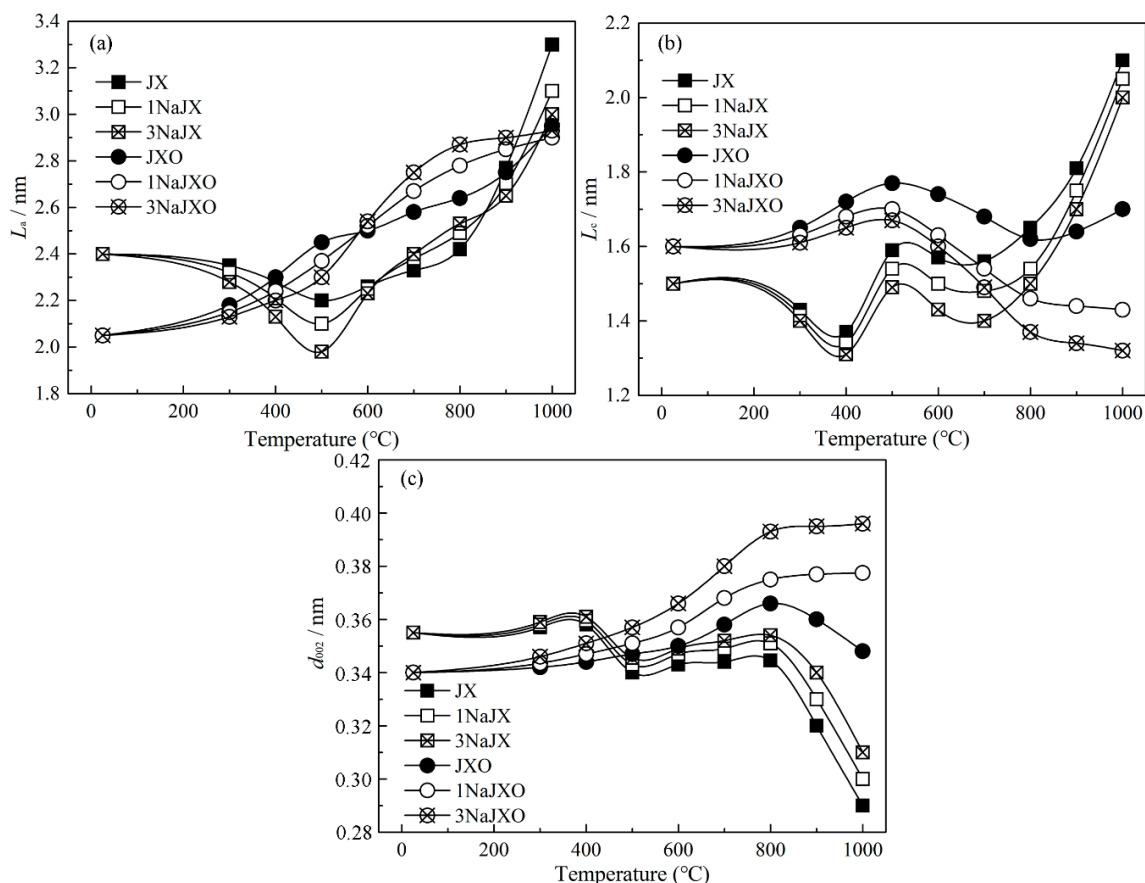


Figure 3. XRD data from chars at pyrolysis (a) L_a ; (b) L_c ; (c) d_{002} .

Then, the values of L_a and d_{002} of JX, 1NaJX and 3NaJX increase and L_c value decrease first and then increase obviously from 500 to 800 °C, these changes may be related to the competition between the break and production of cross-linking bonds. Some disordered aromatic structure units are formed by cross-linking reaction of aromatic layers, resulting in the disordered array and connection of aromatic layers. The formation of stable chemical bonds (CM-Na) at a high temperature cannot only enlarge the spacing of aromatic layer, but produces more organic fragments to increase the amount of cross-linking bonds [43]. However, the presence of more ordered aromatic structure units facilitates the break of chemical bonds instead of the cross-linking reaction of aromatic layers, presenting a graphitization tendency. Alternatively, the values of L_a and d_{002} increase of JXO, 1NaJXO and 3NaJXO, and L_c value decrease with the increase of Na loading. The break of cross-linking bonds with low thermal stability promotes the depolymerization of aromatic layers, and the production of new cross-linking bonds with high thermal stability helps the formation of more aromatic rings with disordered structure. The retention of a large number of Na enhances further the break and formation of cross-linking bonds with different thermal stability, presenting the obvious non-graphitized tendency.

Finally, the values of L_a , L_c and N of JX, 1NaJX, 3NaJX and JXO increase and the d_{002} value decreases rapidly from 800 to 1000 °C. These changes indicate the microcrystalline structure has transformed into a highly ordered graphite-like structure, and the ordered stacking and rapid growth

of aromatic layers are presented at higher pyrolysis temperature. The variation of these parameters can be weakened with the increase of Na loading or the existence of oxygen-containing structures, but it is not easy to hinder the ordered condensation of aromatic layers at a high temperature. Remarkably, the values of L_a and d_{002} of 1NaJXO and 3NaJXO increase gently and the values of L_c gradually decrease, these results indicate that the coexistence of oxygen-containing structures and Na can help further the disordered transformation of aromatic structures at high temperature.

3.4. Specific Surface Area (S_{BET}) Analysis of Coal Chars at Pyrolysis

The value of S_{BET} and V_t of chars is shown in Table 2. First of all, the S_{BET} value of JX increases first slightly and then decreases rapidly from 25 to 500 °C. The formation of pores is related to the release of volatile matter at the beginning of pyrolysis, but the increase of pore volume is limited. With the increase of pyrolysis temperature, a large number of metaplast materials are formed to block the pores of chars. However, the release of more volatile matter and the formation of fewer metaplast materials are performed with the increase of Na loading, leading to the relatively developed pore structure of 1NaJX and 3NaJX compared to that of JX. Alternatively, the S_{BET} value of JXO, 1NaJXO and 3NaJXO increases continuously with the increase of Na loading. The depolymerization and recombination of aromatic structure promote the release of volatile matter and disordered stacking of aromatic layers, and there are no metaplast materials to block the pores for oxidized coal, resulting in the development of the pore. In addition, the depolymerization and cross-linking recombination of aromatic structure can be strengthened under the existence of Na, therefore, the pores structure of 1NaJXO and 3JXNaO can be developed further.

Table 2. The value of S_{BET} (m^2/g) of chars at pyrolysis.

°C S_{BET} Samples	JX	1NaJX	3NaJX	JXO	1NaJXO	3NaJXO
25	21	21	21	54	54	54
300	25	29	33	67	78	83
400	35	40	47	75	87	94
500	8	12	14	84	100	114
600	16.4	19	23	97	115	126
700	27.3	35.6	38.6	111	134	149
800	42	50	55	133	156	167
900	29	32	34	110	150	162
1000	18	24	27	84	141	155

Then, the S_{BET} value of JX, 1NaJX and 3NaJX increases from 500 to 800 °C. The formation of cross-linking bonds between aromatic layers at this condensation stage promotes the production of pores. However, the pores have never been fully developed, due to blockage of metaplast materials. Alternatively, the S_{BET} value of JXO, 1NaJXO and 3NaJXO increases obviously with the increase of Na. The break of oxygen-containing functional groups and oxygen heterocycles promotes the formation of cross-linking bonds and the release of volatile matter, resulting in the disordered condensation of aromatic structure and the formation of more pores. These processes can be strengthened further with the increase of Na loading.

Finally, the S_{BET} value of JX, 1NaJX, 3NaJX, JXO decreases obviously from 800 to 1000 °C. This result is related to the collapse and expansion of microporous to form mes- or macropore and the further collapse of mesopore and macropore can be presented at higher pyrolysis temperature. However, it is difficult to prevent the collapse of pores only in the presence of Na or oxygen-containing functional groups. Remarkably, the S_{BET} value of 1NaJXO and 3NaJXO indicates that the coexistence of oxygen-containing structures and Na can stabilize and develop the three-dimensional spatial structure of aromatic layers, thus resulting in the sustained development of porosity.

3.5. Crystal Structure Analysis of Typical Chars During Activation

3NaJXO-800 is the most suitable precursor for subsequent activation, due to its disordered carbon structure, abundant initial pores and active sites. JX-800 and JXO-800 are used as the contrastive precursor. Therefore, the change of the physicochemical structure for these typical chars during activation can be analyzed in detail. The XRD profiles and crystal parameters of JX-800, JXO-800 and 3NaJXO-800 at different burn offs are shown in Figure S4 and Table 3.

Table 3. XRD data of typical chars at different burn offs.

Samples	L_a (Å)	L_c (Å)	d_{002} (Å)	$N = L_c/d_{002}$
JX-800	24.20	16.50	3.45	4.78
JX-800-19.5	24.66	16.25	3.38	4.81
JX-800-29.1	26.07	17.06	3.30	5.17
JX-800-51.3	27.64	18.27	3.11	5.87
JXO-800	26.40	16.20	3.66	4.43
JXO-800-19.7	26.13	16.01	3.71	4.31
JXO-800-29.4	26.04	15.77	3.78	4.17
JXO-800-47.2	26.98	16.51	3.58	4.61
3NaJXO-800	28.70	13.70	3.93	3.48
3NaJXO-800-19.3	27.55	13.49	4.01	3.36
3NaJXO-800-29.2	27.36	13.11	4.15	3.16
3NaJXO-800-48.1	27.18	12.77	4.23	3.02

First of all, there is a sustained increase in the values of L_a and N of JX-800 and decrease in the d_{002} value, however, the L_c value first decreases from 0 to 19.5% and then increases from 19.5 to 51.3%. These changes indicate that the microcrystalline of JX-800 always develops towards a highly ordered structure during activation. At the beginning of activation, the reaction between activated gas and the active sites and some sandwich materials in the longitudinal aromatic layers results in a decrease in the values of d_{002} and L_c . With an increase in carbon loss, the aromatic layers with the more ordered orientation rapidly begin to condense and distort that promotes the thickness and size of the microcrystalline.

Alternatively, the values of L_c , L_a and N of JXO-800 first decrease and then increase, whereas d_{002} value first increases and then decreases with an increase in burn offs. These changes indicate that the existence of oxygen-containing structure of JXO-800 may hinder the ordered transformation of aromatic layers at the beginning of activation. More active sites (including the defects and the oxygen-containing side chains and bridge of basic unit in aromatic layers) are removed by activated gas to strengthen the etching of carbon-based framework, thus resulting in the decrease of the thickness and size of the microcrystalline structure. With an increase in carbon loss, the more active sites of JXO-800 have been consumed, therefore the horizontal and longitudinal condensation of aromatic layers have been presented; moreover, the rapid reduction of lamellar spacing also indicates the highly ordered transformation of aromatic structures.

Finally, there is a sustained decrease in values of L_a , L_c and N of 3NaJXO-800 and the increase on d_{002} value during activation, indicating that the addition of Na catalyst has promoted a continuous disordered conversion of aromatic structures. The distortion of the longitudinal aromatic structure can accompany with its catalytic cracking, thus resulting in an obvious decrease in the L_c value. Na bonded and fixed in carbon matrix may destroy the parallelism of the layer and the constancy of the interlayer spacing, thus increasing the interlayer spacing; however, Na-based compounds can further accelerate the etching of aromatic layer instead of their ordered condensation and growth.

3.6. Carbon Structure Analysis of Typical Chars During Activation

The Raman spectra and corresponding parameters and of JX-800, JXO-800 and 3NaJXO-800 at different burn offs are shown in Figure S5 and Table 4.

Table 4. Raman data of typical chars at different burn offs.

Samples	A_{D1}/A_G	A_{D3}/A_G	A_{D4}/A_G	A_{D1}/A_{D3}
JX-800	2.36	0.91	0.69	2.60
JX-800-19.5	2.92	0.83	0.58	3.52
JX-800-29.1	3.68	0.78	0.39	4.72
JX-800-51.3	1.81	0.53	0.11	3.42
JXO-800	2.98	1.21	1.01	2.48
JXO-800-19.7	2.87	1.28	1.19	2.24
JXO-800-29.4	2.80	1.32	1.23	2.12
JXO-800-47.2	2.71	1.01	0.99	2.68
3NaJXO-800	3.75	1.47	1.50	2.55
3NaJXO-800-19.3	3.70	1.55	1.57	2.39
3NaJXO-800-29.2	3.61	1.64	1.69	2.20
3NaJXO-800-48.1	3.53	1.79	1.74	1.97

There is a sustained decrease in the values of A_{D3}/A_G and A_{D4}/A_G , and the values of A_{D1}/A_G and A_{D1}/A_{D3} first increase at the low burn offs and then decrease at the high burn offs. At the beginning of activation, the active sites are consumed by activated gas preferentially, resulting in a decrease in the A_{D3}/A_G and A_{D4}/A_G values. In addition, the growth and conversion of aromatic ring and its conversion into big aromatic ring structures promote the increase in the A_{D1}/A_{D3} and A_{D1}/A_G values. With an increase in burn-offs, the interior of aromatic structure can be activated by the continuous penetration of the activated gas to further induce the condensation of the aromatic ring [42]. Alternatively, there is a sustained decrease in A_{D1}/A_G value of JXO-800, whereas the values of A_{D3}/A_G and A_{D4}/A_G first increases and then decreases, and the A_{D1}/A_{D3} value first decreases and then increases. At the beginning of activation, the existence of more active sites promotes further the etching of carbon structure, thus hindering its growth. In addition, the existence of more oxygen-containing structure facilitates the production of new cross-linking bonds and small aromatic ring, but the reaction path between active sites and active gas still can't be changed. With an increase in burn-offs, consistent reduction of oxygen-containing structure and self-consumption of the small aromatic ring and its conversion into a big aromatic ring are presented to promote the formation of more crystalline sp^2 structure. Finally, there is a sustained decrease in the values of A_{D1}/A_{D3} and A_{D1}/A_G of 3NaJXO-800 and the increase in the values of A_{D3}/A_G and A_{D4}/A_G . It can be inferred that the presence of Na catalyst can change the reaction pathways between the carbon structure and activated gas. More concretely, the active sites can no longer be consumed with activated gas preferentially, and the big aromatic rings would begin to decompose into small aromatic rings and the Na catalyst also hinder the formation of the crystalline sp^2 structure. In other words, a large number of broken fragments are produced by the catalytic effect of Na, resulting in the formation of newer cross-linking structure. Moreover, the presence of oxygen-containing structures is conducive to the reorganization of aromatic fragments.

3.7. Pore Structure Development of Typical Chars During Activation

To analyze the pore development of JX-800, JXO-800 and 3NaXO-800 at different burn-off values during activation, N_2 adsorption isotherms and parameters of porous structure are shown in Figure 4 and Table 5.

First of all, the S_{BET} value of $101.78 \text{ m}^2 \cdot \text{g}^{-1}$, V_{mic} value of $0.06 \text{ m}^3 \cdot \text{g}^{-1}$ and non- V_{mic} value of 6.25% of JX-800-19.5 are obtained, showing the development of micropores at the beginning of activation. These values increase gradually with an increase in burn-offs from 19.5% to 51.3%, that are related to the enlargement of micropores into mesopores and the production of some new micropores. Remarkably, the rapid increase of non- V_{mic} value indicates the more obvious development of mesopore rather than that of new micropores. At a higher burn offs, an $S_{BET}/\text{burn-off}$ ratio value of $13.23 \text{ m}^2 \text{ g}^{-1}/\%$ of JX-800-51.3 is obtained. Many macropores from $2 \mu\text{m}$ to $35 \mu\text{m}$ on the particle surfaces can be found in JX-800-51.3 from Figure 5a, indicating the severe carbon losses on the particle surfaces during

activation. This result may be related with the ordered conversion of the aromatic structure of JX-800 with less initial pores can hinder the penetration of activated gas into the interior of char structure during activation, thus resulting in the occurrence of more reactions on the particle surfaces rather than in the interior to decrease the production of the pores.

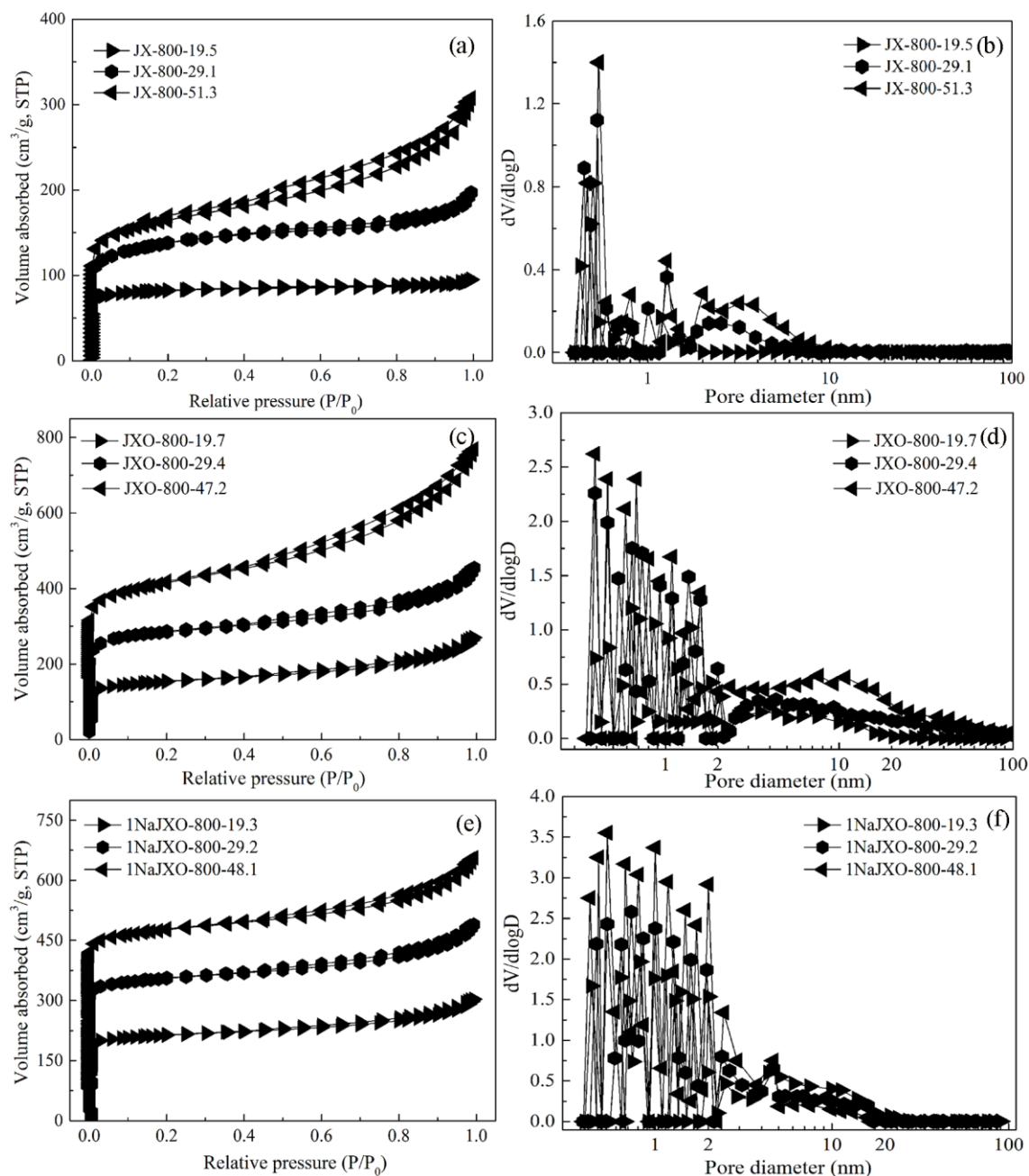


Figure 4. N_2 adsorption isotherms (a), (c) (e) and pore-size distributions (b), (d) (f) of activated carbons at different burn offs.

Then, the increase in V_t , V_{mic} and S_{BET} values and the decrease in the non- V_{mic} value of JXO-800 with the increase of burn offs from 0 to 29.4% show an obvious growth of micropores. These changes are related to the initial pores of JXO-800 act as channels to promote the diffusion of activated gas and more active sites produced by pyrolysis can strengthen the etching of carbon structure. All pore parameters of JXO-800 increase gradually with the increase of burn offs from 29.4 to 47.2%, indicating the formation of new micropores slows down; however, a rapid development of mesopores mainly results from

the widening of the pores. The oxygen functional groups of JXO-800 as active sites are consumed gradually with continuous activation, resulting in limited micropores development. In particular, an $S_{\text{BET}}/\text{burn-off}$ ratio value of $22.99 \text{ m}^2 \text{ g}^{-1}/\%$ of JXO-800-47.2 is obtained. No severe carbon losses and macropores on the particle surfaces of JXO-800-47.2 are found from Figure 5b, these changes are related to the penetration of activated gas into the interior of the particle during activation.

Table 5. Pore structure parameters of typical chars at different burn offs.

Samples	S_{BET} (m^2/g)	V_t (m^3/g)	V_{mic} (m^3/g)	Non- V_{mic} (%)	$S_{\text{BET}}/\text{Burn offs}$ ($\text{m}^2 \text{ g}^{-1}/\%$)
JX-800	42	0.029	0.020	3.1	-
JX-800-19.5	101.78	0.064	0.060	6.25	5.22
JX-800-29.1	315.78	0.165	0.131	20.61	10.85
JX-800-51.3	678.90	0.285	0.175	38.59	13.23
JXO-800	133	0.101	0.059	41.58	-
JXO-800-19.7	352.78	0.189	0.132	30.16	17.91
JXO-800-29.4	648.21	0.297	0.247	16.84	22.05
JXO-800-47.2	1085.53	0.356	0.278	21.91	22.99
3NaJXO-800	167	0.199	0.132	33.67	-
3NaJXO-800-19.3	659.35	0.310	0.245	20.97	34.16
3NaJXO-800-29.2	1156.57	0.378	0.310	17.99	39.61
3NaJXO-800-48.1	1995.35	0.481	0.421	12.47	41.48

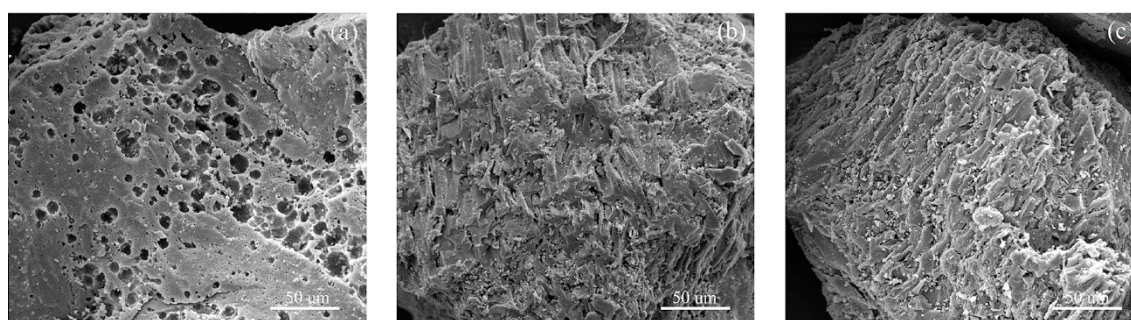


Figure 5. SEM images of typical chars under final burn-off values (a) JX-800-51.3; (b) JXO-800-47.2; (c) 3NaJXO-800-48.1.

Finally, the rapid increase in V_t , V_{mic} and S_{BET} values and the rapid decrease in non- V_{mic} value of 3NaJXO-800 during the whole stage of activation are shown in Table 5. Along with the gradual consumption of oxygen functional groups, the disordered conversion of carbon structure and more active sites in the presence of Na-based catalysts facilitate a sustained formation of more micropores. Although the catalysts might have moved and agglomerated on the particle surfaces with an increase of burn-off at high temperature activation, the simultaneous existence of oxygen functional groups and Na-based catalyst can constantly enhance the development of micropores. Importantly, an $S_{\text{BET}}/\text{burn-off}$ ratio value of $41.48 \text{ m}^2 \text{ g}^{-1}/\%$ of 3NaJXO-800-48.1 is obtained. Moreover, the surface morphology of 3NaJXO-800-48.1 is similar to that of JXO-800-47.2 from Figure 5c, indicating no severe carbon losses on the particle surfaces of 3NaJXO-800-48.1.

3.8. Study of SO_2 Adsorption

The SO_2 adsorption test from a simulated flue gas in which JX-800-51.3, JXO-800-47.2 and 3NaJXO-800-48.1 as testing samples is carried out under 80°C , the result of SO_2 removal of the samples is shown in Figure 6.

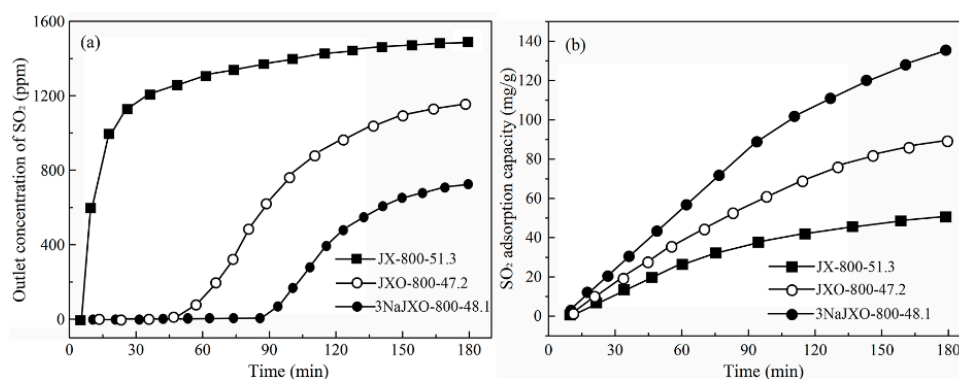


Figure 6. SO₂ removal of typical activated carbon (a) SO₂ breakthrough curve; (b) SO₂ adsorption quantity.

The SO₂ adsorption capacities of JX-800-51.3 are mainly exhibited within only 30 min, after that, its desulfurization performance is obviously reduced from 30 to 180 min. The SO₂ concentrations of gas outlet for JX-800-51.3 have achieved 1200 ppm about 30 min, showing that it has been penetrated basically by SO₂. The SO₂ adsorption capacity of JX-800-51.3 can only achieve 50.2 mg/g. Then SO₂ adsorption efficiency of 3NaJXO-800-48.1 maintains at 100% within 90 min. The SO₂ concentrations of gas outlet for 3NaJXO-800-48.1 slowly increase from 90 to 180 min and only achieve 700 ppm at 180 min, indicating the adsorptive capacity of 3NaJXO-800-48.1 with 140.2 mg/g is still strong. However, the SO₂ adsorption capacities of JXO-800-47.2 are presented between JX-800-51.3 and 3NaJXO-800-48.1. In the case of AC, the hierarchical structure (micro- and mesopores) is critical to the SO₂ removal process, the adsorption and catalysis processes of SO₂ are performed within the micropores, and the developed mesopores promote the migration and storage of produced sulfuric acid [3]. In addition, a high specific surface area (S_{BET}), which is related to the degree of well-developed pores, promotes desulfurization [44]. In addition, Zhu et al. [16,17] found that with the increase of burnout rate, the amount of basic functional groups has a good positive correlation with micropore. When the micropore originates from the microcrystalline structure etched by activated gas, they have a better linear relationship. The more active sites and high micropore volume of 3NaJXO-800-48.1 promote the adsorption and catalysis processes of SO₂ within the micropores, then a well-developed mesopore is conducive to the migration and storage of sulfuric acid to release consistently the active sites as adsorption sites within the micropores, which ensures the persistent adsorption capacity. However, the SO₂ adsorption capacities of JX-800-51.3 has reached saturation quickly in the initial stage, due to its less active sites and low micropores value, then undeveloped mesopore of JX-800-51.3 is unable to meet the storage of more sulfuric acid to release consistently the active sites, thus presenting a low SO₂ adsorption capacity.

4. Conclusions

A catalytic effect of NaCl (1 and 3 wt%) in presence of oxygen functional groups (created by air pre-oxidation at 200 °C for 48 h) has provided control of the physicochemical structure of Jixi bituminous coal-based ACs for high efficiency of SO₂ adsorption. In the phase of pyrolysis, a large number of Na catalyst can be fixed first in the interior of chars by the oxygen functional groups in the form of some intermediates (such as -O-Na and -COONa), then Na can be re-bonded with carbon matrix (CM-Na) at high temperatures, during which the catalytic cracking characteristics of Na catalyst plays a more important role, finally resulting in the disordered conversion of microstructure and the number of more active sites. Moreover, Na catalyst also helps the development of micropores; however, the evolution of oxygen functional groups mainly facilitates the production of mesopores. In the phase of activation, the reaction pathway of active sites and CO₂ was changed by the presence of Na catalyst, leading to a consistent disordered conversion of the microstructure and the production of new active sites of 3NaXO-800. With an increase in burn offs, the existence of Na catalyst facilitates the etching of

the carbon structure to develop continuously the micropores rather than only widening of the pores to form mesopore and macropore. Finally, the S_{BET} values ($1995.35 \text{ m}^2 \cdot \text{g}^{-1}$) of 3NaXO-800-48.1 with the high S_{BET} /burn-off ratio values of $41.48 \text{ m}^2 \cdot \text{g}^{-1}/\%$. is obtained, presenting a persistent high adsorption efficiency (100%) within 90 min and a high SO_2 adsorption capacity with 140.2 mg/g after 180 min.

Supplementary Materials: The following are available online at <http://www.mdpi.com/2227-9717/7/6/338/s1>, Figure S1: Schematic figure of the fixed bed reactor system for SO_2 adsorption, Figure S2: Raman spectra from chars produced by pyrolysis, Figure S3: XRD profiles from chars produced by pyrolysis, Figure S4: XRD profiles of coal chars at different burn offs during activation (a) JX-800; (b) JXO-800; (c) 3NaJXO-800; Figure S5: Raman spectra of coal chars at different burn offs during activation (a) JX-800; (b) JXO-800; (c) 3NaJXO-800.

Author Contributions: D.L., B.J. and L.D. conceived and designed the experiments; X.Z., R.S. and Z.H. carried out the experiments; D.L. wrote the paper; D.L. and B.J. reviewed the paper.

Funding: This research was funded by National Natural Science Foundation of China, grant number 51806080, and Scientific Research Fund Project of Jilin Agricultural University, grant number 201801, and Jilin Province Education Department Science and Technology Program during the Thirteenth Five-year Plan Period, grant number JJKH20190940KJ.

Conflicts of Interest: The authors declare no conflict of interest.

References

1. Srinivas, G.; Zheng, X.G. Graphene-based materials: Synthesis and gas sorption, storage and separation. *Prog. Mater. Sci.* **2015**, *69*, 1–60. [[CrossRef](#)]
2. Bahamon, D.; Vega, L.F. Systematic evaluation of materials for post-combustion CO_2 capture in a temperature swing adsorption process. *Chem. Eng. J.* **2016**, *284*, 438–447. [[CrossRef](#)]
3. Shu, S.; Guo, J.X.; Liu, X.L.; Wang, X.J.; Yin, H.Q.; Luo, D.M. Effects of pore sizes and oxygen-containing functional groups on desulfurization activity of Fe/NAC prepared by ultrasonic-assisted impregnation. *Appl. Surf. Sci.* **2016**, *360*, 684–692. [[CrossRef](#)]
4. Hong, K.L.; Long, Q.; Zeng, R. Biomass derived hard carbon used as a high performance anode material for sodium ion batteries. *J. Mater. Chem. A* **2014**, *2*, 12733–12738. [[CrossRef](#)]
5. Nishihara, H.; Kyotani, T. Templated nanocarbons for energy storage. *Adv. Mater.* **2012**, *24*, 4473–4498. [[CrossRef](#)]
6. He, X.J.; Li, R.C.; Qiu, J.S.; Xie, K.; Ling, P.H.; Yu, M.X.; Zhang, X.Y.; Zheng, M.D. Synthesis of mesoporous carbons for supercapacitors from coal tar pitch by coupling microwave-assisted KOH activation with a MgO template. *Carbon* **2012**, *50*, 4911–4921. [[CrossRef](#)]
7. Hu, B.; Wang, K.; Wu, L.H.; Yu, S.H.; Antonietti, M.; Titirici, M.M. Engineering carbon materials from the hydrothermal carbonization process of biomass. *Adv. Mater.* **2010**, *22*, 813–828. [[CrossRef](#)]
8. Sun, F.; Wu, H.B.; Liu, X.; Liu, F.; Zhou, H.H.; Gao, J.H.; Lu, Y.F. Nitrogen-rich carbon spheres made by a continuous spraying process for high-performance supercapacitors. *Nano Res.* **2016**, *9*, 3209–3221. [[CrossRef](#)]
9. Alabad, A.; Razzaque, S.; Yang, Y.W.; Chen, S.; Tan, B. Highly porous activated carbon materials from carbonized biomass with high CO_2 capturing capacity. *Chem. Eng. J.* **2015**, *281*, 606–612. [[CrossRef](#)]
10. Srinivas, G.; Yue, L.; Neal, S.; Taner, Y.; Zheng, X.G. Design of hyperporous graphene networks and their application in solid-amine based carbon capture systems. *J. Mater. Chem. A* **2017**, *5*, 17833–17840. [[CrossRef](#)]
11. Srinivas, G.; Hasmukh, A.P.; Zheng, X.G. Carbon capture: An ultrahigh pore volume drives up the amine stability and cyclic CO_2 capacity of a solid-amine@carbon sorbent. *Adv. Mater.* **2015**, *27*, 4903–4909. [[CrossRef](#)]
12. Teng, H.; Ho, J.A.; Hsu, Y.F. Preparation of activated carbons from bituminous coals with CO_2 activation-Influence of coal oxidation. *Carbon* **1997**, *35*, 275–283. [[CrossRef](#)]
13. Teng, H.; Ho, J.A.; Hsu, Y.F.; Hsieh, C.T. Preparation of activated carbons from bituminous coals with CO_2 activation. 1. effects of oxygen content in raw coals. *Fuel Energy Abstr.* **1996**, *38*, 139–146. [[CrossRef](#)]
14. Akash, B.A.; O'Brien, W.S. The production of activated carbon from a bituminous coal. *Int. J. Energy Res.* **1996**, *20*, 913–922. [[CrossRef](#)]
15. San, M.G.; Fowler, G.D.; Sollars, C.J. A study of the characteristics of activated carbons produced by steam and carbon dioxide activation of waste tyre rubber. *Carbon* **2003**, *41*, 1009–1061. [[CrossRef](#)]

16. Zhu, Y.W.; Gao, J.H.; Li, Y.; Sun, F. Preparation of activated carbons for SO₂ adsorption by CO₂ and steam activation. *J. Taiwan Inst. Chem. Eng.* **2012**, *43*, 112–119. [[CrossRef](#)]
17. Zhu, Y.W.; Gao, J.H.; Li, Y.; Sun, F.; Qin, Y.K. Preparation and characterization of activated carbons for SO₂ adsorption from taixi anthracite by physical activation with steam. *Korean J. Chem. Eng.* **2011**, *28*, 2344–2350. [[CrossRef](#)]
18. Liu, D.D.; Gao, J.H.; Wu, S.H.; Qin, Y.K. Effect of char structures caused by varying the amount of FeCl₃ on the pore development during activation. *RSC Adv.* **2016**, *6*, 87478–87485. [[CrossRef](#)]
19. Coetzee, S.; Neomagus, H.; Bunt, J.R. Improved reactivity of large coal particles by K₂CO₃ addition during steam gasification. *Fuel Process. Technol.* **2013**, *114*, 75–80. [[CrossRef](#)]
20. Fan, S.M.; Yuan, X.Z.; Park, J.C.; Xu, L.H.; Kang, T.J.; Kim, H.T. Gasification of Indonesian sub-bituminous coal with different gasifying agents using Ca and K catalysts. *Energy Fuels* **2016**, *30*, 9372–9378. [[CrossRef](#)]
21. Kopyscinski, J.; Habibi, R.; Mims, C.A. K₂CO₃-catalyzed CO₂ gasification of ash-free coal: Kinetic study. *Energy Fuels* **2013**, *27*, 4875–4883. [[CrossRef](#)]
22. Kim, H.S.; Kudo, S.; Tahara, K.; Hachiyama, Y.; Yang, H.; Norinaga, K.; Hayashi, J.I. Detailed kinetic analysis and modeling of steam gasification of char from Ca-loaded lignite. *Energy Fuels* **2013**, *27*, 6617–6631. [[CrossRef](#)]
23. Zhang, L.; Kudo, S.; Tsubouchi, N.; Hayashi, J.I.; Ohtsuka, Y.; Norinaga, K. Catalytic effects of Na and Ca from inexpensive materials on in-situ steam gasification of char from rapid pyrolysis of low rank coal in a drop-tube reactor. *Fuel Process. Technol.* **2013**, *113*, 1–7. [[CrossRef](#)]
24. Olsson, J.G.; Jaglid, U.; Petterson, J.B.C.; Hald, P. Alkali metal emission during pyrolysis of biomass. *Energy Fuels* **1997**, *11*, 779–784. [[CrossRef](#)]
25. Kowalski, T.; Ludwig, C.; Wokaun, A. Qualitative evaluation of alkali release during the pyrolysis of biomass. *Energy Fuels* **2007**, *21*, 3017–3022. [[CrossRef](#)]
26. Li, C.Z.; Sathe, C.; Kershaw, J.R.; Pang, Y. Fates and roles of alkali and alkaline earth metals during the pyrolysis of a victorian brown coal. *Fuel* **2000**, *79*, 427–438. [[CrossRef](#)]
27. Keown, D.M.; Favas, G.; Hayashi, J.; Li, C.Z. Volatilisation of alkali and alkaline earth metallic species during the pyrolysis of biomass: Differences between sugar cane bagasse and cane trash. *Bioresour. Technol.* **2005**, *96*, 1570–1577. [[CrossRef](#)]
28. Matsuoka, K.; Yamashita, T.; Kuramoto, K.; Suzuki, Y.; Takaya, A.; Tomita, A. Transformation of alkali and alkaline earth metals in low rank coal during gasification. *Fuel* **2008**, *87*, 885–893. [[CrossRef](#)]
29. Sun, X.; Li, Y. Ga₂O₃ and GaN semiconductor hollow spheres. *Angew. Chem.* **2004**, *116*, 3915–3919. [[CrossRef](#)]
30. Sugano, M.; Mashimo, K.; Wainai, T. Structural changes of lower rank coals by cation exchange. *Fuel* **1999**, *78*, 945–951. [[CrossRef](#)]
31. Gorrini, B.C.; Radovic, R.C.; Gordonb, A.L. On the potassium-catalysed gasification of a chilean bituminous coal. *Fuel* **1990**, *69*, 789–791. [[CrossRef](#)]
32. Liu, D.D.; Gao, J.H.; Cao, Q.X.; Wu, S.H.; Qin, Y.K. Improvement of activated carbon from Jixi bituminous coal by air preoxidation. *Energy Fuels* **2017**, *31*, 1406–1415. [[CrossRef](#)]
33. Heras, F.; Alonso-Morales, N.; Jimenez-Cordero, D.; Gilarranz, M.A.; Rodriguez, J.J. Granular mesoporous activated carbons from waste tires by cyclic oxygen chemisorption-desorption. *Ind. Eng. Chem. Res.* **2012**, *51*, 2609–2614. [[CrossRef](#)]
34. Gong, X.Z.; Guo, Z.C.; Wang, Z. Variation of char structure during anthracite pyrolysis catalyzed by Fe₂O₃ and its influence on char combustion reactivity. *Energy Fuels* **2009**, *23*, 4547–4552. [[CrossRef](#)]
35. Yang, K.B.; Peng, J.H.; Xia, H.Y.; Zhang, L.B.; Srinivasakannan, C.; Guo, S.H. Textural characteristics of activated carbon by single step CO₂ activation from coconut shells. *J. Taiwan Inst. Chem. Eng.* **2010**, *41*, 367–372. [[CrossRef](#)]
36. Karatepe, N.; Orbak, İ.; Yavuz, R.; Özyuğuran, A. Sulfur dioxide adsorption by activated carbons having different textural and chemical properties. *Fuel* **2008**, *87*, 3207–3215. [[CrossRef](#)]
37. Sun, F.; Gao, J.H.; Liu, X.; Yang, Y.Q.; Wu, S.H. Controllable nitrogen introduction into porous carbon with porosity retaining for investigating nitrogen doping effect on SO₂ adsorption. *Chem. Eng. J.* **2015**, *290*, 116–124. [[CrossRef](#)]
38. Sathe, C.; Pang, Y.; Li, C.Z. Effects of heating rate and ion-exchangeable cations on the pyrolysis yields from a Victorian brown coal. *Energy Fuels* **1999**, *13*, 748–755. [[CrossRef](#)]

39. Li, T.; Zhang, L.; Li, D. Effects of gasification atmosphere and temperature on char structural evolution during the gasification of collie sub-bituminous coal. *Fuel* **2014**, *117*, 1190–1195. [[CrossRef](#)]
40. Sasezky, A.; Muckenhuber, H.; Grothe, H. Raman microspectroscopy of soot and related carbonaceous materials: Spectral analysis and structural information. *Carbon* **2005**, *43*, 1731–1742. [[CrossRef](#)]
41. He, X.F.; Jin, L.J.; Wang, D.; Zhao, Y.P.; Zhu, S.W.; Hu, H.Q. Integrated process of coal pyrolysis with CO₂ reforming of methane by dielectric barrier discharge plasma. *Energy Fuels* **2011**, *25*, 4036–4042. [[CrossRef](#)]
42. Li, W.; Zhu, Y.M. Structural characteristics of coal vitrinite during pyrolysis. *Energy Fuels* **2014**, *28*, 3645–3654. [[CrossRef](#)]
43. Liu, H.; Xu, L.F.; Zhao, D.; Cao, Q.X.; Gao, J.H.; Wu, S.H. Effects of alkali and alkaline-earth metals and retention time on the generation of tar during coal pyrolysis in a horizontal fixed-bed reactor. *Fuel Process. Technol.* **2018**, *179*, 399–406. [[CrossRef](#)]
44. Lizzio, A.A.; Debarr, J.A. Effect of surface area and chemisorbed oxygen on the SO₂ adsorption capacity of activated char. *Fuel* **1996**, *75*, 1515–1522. [[CrossRef](#)]



© 2019 by the authors. Licensee MDPI, Basel, Switzerland. This article is an open access article distributed under the terms and conditions of the Creative Commons Attribution (CC BY) license (<http://creativecommons.org/licenses/by/4.0/>).